

# Munc18-1 Protein Molecules Move between Membrane Molecular Depots Distinct from Vesicle Docking Sites<sup>\*[5]</sup>

Received for publication, August 8, 2012, and in revised form, November 5, 2012. Published, JBC Papers in Press, December 7, 2012, DOI 10.1074/jbc.M112.407585

Annya M. Smyth<sup>‡§</sup>, Lei Yang<sup>¶</sup>, Kirsty J. Martin<sup>‡</sup>, Charlotte Hamilton<sup>‡</sup>, Weiping Lu<sup>‡</sup>, Michael A. Cousin<sup>§</sup>, Colin Rickman<sup>‡1</sup>, and Rory R. Duncan<sup>‡1,2</sup>

From the <sup>‡</sup>Life-Physical Sciences Interface Laboratory, Institute of Biological Chemistry, Biophysics and Bioengineering, School of Engineering and Physical Sciences, Heriot Watt University, Edinburgh EH14 4AS, Scotland, United Kingdom, the <sup>§</sup>Centre for Integrative Physiology, University of Edinburgh, George Square, Edinburgh EH8 9XD, Scotland, United Kingdom, and <sup>¶</sup>Philips Research Asia, Philips Innovation Campus, Tianlin Road, Shanghai 200233, China

**Background:** The molecular architecture of the secretory machinery is undefined.

**Results:** Munc18 moves between membrane depots distinct from vesicle docking sites.

**Conclusion:** Munc18 is not a docking factor, and the membrane environment is likely to determine fusion likelihood.

**Significance:** It is now possible to test directly previous models of the molecular mechanisms of secretion.

Four evolutionarily conserved proteins are required for mammalian regulated exocytosis: three SNARE proteins, syntaxin, SNAP-25, and synaptobrevin, and the SM protein, Munc18-1. Here, using single-molecule imaging, we measured the spatial distribution of large cohorts of single Munc18-1 molecules correlated with the positions of single secretory vesicles in a functionally rescued Munc18-1-null cellular model. Munc18-1 molecules were nonrandomly distributed across the plasma membrane in a manner not directed by mode of interaction with syntaxin1, with a small mean number of molecules observed to reside under membrane resident vesicles. Surprisingly, we found that the majority of vesicles in fully secretion-competent cells had no Munc18-1 associated within distances relevant to plasma membrane-vesicle SNARE interactions. Live cell imaging of Munc18-1 molecule dynamics revealed that the density of Munc18-1 molecules at the plasma membrane anticorrelated with molecular speed, with single Munc18-1 molecules displaying directed motion between membrane hotspots enriched in syntaxin1a. Our findings demonstrate that Munc18-1 molecules move between membrane depots distinct from vesicle morphological docking sites.

The tight temporal and spatial control of membrane fusion is dependent on the action of the three SNARE proteins, syntaxin, SNAP-25, and synaptobrevin (1), and their Sec/Munc protein regulator, Munc18-1 (2). Munc18-1 can interact with its cognate syntaxin in two distinct conformations; it can bind and stabilize syntaxin in a closed conformation in which the Habc domain of syntaxin folds back and occludes the SNARE motif (2, 3) and via its highly conserved N terminus (4–7). To date, Munc18-1 has been ascribed a wide range of functions; it has

been shown to promote the docking of large dense core vesicles (8) and to regulate the “primed” state of synaptic vesicles (9, 10) and both the stabilization and the stimulation of SNARE complex assembly immediately prior to vesicle fusion (3, 5, 11, 12). As well as acting at the end point of the exocytosis process, Munc18-1 is accepted to act as a key factor in the trafficking of syntaxin1 to the plasma membrane (13–15), by preventing the formation of ectopic SNARE complexes (16). Despite these advances, however, it remains unknown how Munc18-1 is spatially arranged and dynamically regulated at the molecular level to execute its functions. The development of techniques specifically for imaging single molecules in living cells provides an insight into local membrane environments by dissecting heterogeneities in molecular behavior. To date, single particle tracking has helped to elucidate the molecular kinetics behind a number of cellular events, including, for example, the movement of myosin V over actin filaments (17) to the membrane binding mechanisms of epidermal growth factors (18). More recently, the use of photoactivatable markers in conjunction with single particle tracking has enabled the quantification of the diffusion coefficient of tens of thousands of hemagglutinin molecules in living fibroblast cells (19). Here, we applied single-molecule imaging approaches and statistical analyses to define the molecular arrangement and kinetics of large cohorts of single Munc18-1 molecules in relation to single vesicles across the plasma membrane of intact cells.

## MATERIALS AND METHODS

### Vectors and Cell Culture

A plasmid encoding a polyhistidine-tagged Munc18-1 (amino acids 1–594) and Munc18-1[I127A] was as described previously (20, 21). The I127A mutation was generated by site-directed mutagenesis of Munc18-1 in pEYFP-N1 vectors using a QuikChange II XL kit (Stratagene). Munc18-1 siRNA PC-12 cells (KD43) were a kind gift of Shuzo Sugita (15) and grown in RPMI medium supplemented with 10% horse serum, 5% fetal bovine serum, 10 mM GlutaMAX (Invitrogen), 50 μg/ml gentamicin, 2.5 μg/ml puromycin and maintained at 37 °C in 7.5%

<sup>\*</sup> This work was supported by project grants from the Medical Research Council (MRC), the Wellcome Trust, and the Royal Society (to R. R. D. and C. R.) and a Ph. D. studentship award from the MRC (to R. R. D. and M. A. C.).  
<sup>§</sup> Author's Choice—Final version full access.

[5] This article contains supplemental Figs. 1–5.

<sup>1</sup> Both authors contributed equally to this work.

<sup>2</sup> To whom correspondence should be addressed. Tel.: 44-131-451-3414; E-mail: r.r.duncan@hw.ac.uk.

(v/v) CO<sub>2</sub>, 92.5% (v/v) air. Transfections were performed using Lipofectamine 2000 (Invitrogen).

### Fluorescence Microscopy

**Microscope Setup**—All experiments were performed on an inverted IX81 microscope (Olympus) using a 150× 1.45 NA objective. Illumination was provided by a fully motorized four-laser TIRF<sup>3</sup> combiner coupled to 405-, 491-, 561-, and 540-nm 100-milliwatt lasers. This allowed for rapid switching of penetration depth from wide field to TIRF illumination during experiments. The sample was maintained in an environmental chamber (Okolab) at 21 °C for fixed samples or at 37 °C in 5% CO<sub>2</sub>, 95% air for live cells. To minimize lateral drift during acquisition, a nosepiece stage (Olympus) was employed. Lateral drift using this stage was  $\sim \pm 6$  nm over a typical 30-min acquisition. This meant no correction for drift was required after acquisition. This is comparable with the localization accuracy, due to the signal-to-noise ratio of detected single molecules, of 3–10 nm for photoactivatable localization microscopy (PALM) or ground state depletion followed by individual molecule return microscopy (GSDIM) datasets. Fluorescence emission was detected using a 512 × 512-pixel, water-cooled EMCCD camera (Hamamatsu).

**GSDIM**—GSDIM microscopy was performed based on previously described methods (22). Cells were fixed in 4% (w/v) buffered paraformaldehyde for 90 min at room temperature. The extended fixation period is to immobilize as much as possible the molecules under study to minimize potential movement or antibody patching artifacts (23). Permeabilization was with 0.1% Triton X-100 at room temperature for 5 min. Immunodetection and staining of Munc18-1 used 1:1000 dilution of anti-Munc18-1 mouse monoclonal antibody (BD Biosciences 610336) for 3 h followed by anti-mouse IgG Alexa Fluor 647-conjugated secondary antibody (Invitrogen, 1:1000–1:2000 dilution). All antibodies and washes were in the presence of 0.1% fish skin gelatin (Sigma) and 0.1% Tween 20 to block non-specific binding. Controls where no primary antibody was added resulted in no detectable signal using the imaging parameters (laser power, EM gain) employed (see below). Cells were not mounted for imaging but instead were imaged in photo-bleached and filtered (0.22 micron) PBS. To ensure efficient switching of Alexa Fluor 647, cells were imaged in 0.5 mg/ml glucose oxidase, 40 μg/ml catalase, 10% w/v glucose, and 50 mM β-mercaptoethylamine. In a typical experiment, cells were initially excited by 491-nm laser light under TIRF illumination to acquire anti-synaptotagmin 1 (polyclonal; SySy, 1:2000 dilution of primary antibody)-labeled, Alexa Fluor 488-detected vesicle fluorescence. The cell was then continuously illuminated with 640-nm laser light ( $\sim 10$ – $12$  milliwatts at the sample) under TIRF illumination for 15–30 min. Emitted fluorescence was detected using an EMCCD camera with an EM gain of 100–500

and a frame rate of 20 Hz. The resulting image sequences were subsequently analyzed using single-molecule identification and localization algorithms described below. The repeated cycling of fluorophores between the excited and dark states results in repetitive localization of the same fluorophore multiple times. The precise distances between the Alexa Fluor 647 fluorophore molecule and the epitope are difficult to estimate, and there are multiple fluorophores on each secondary antibody; however, these distances are likely to be <15 nm, based on the average diameter of an immunoglobulin of 7 nm.

**PALM**—PALM microscopy was performed based on previously described methods (24, 25). Cells, expressing photoactivatable mCherry-labeled SNAREs, were fixed and immunostained as required, as detailed above. Cells were imaged in PBS at 21 °C. In a typical experiment, cells were initially excited by 491-nm laser light under TIRF illumination to acquire Alexa Fluor 488- or GFP-labeled vesicle fluorescence. Photoactivatable mCherry was then activated with a brief pulse (1–250 ms) of 405-nm laser light under TIRF illumination followed by acquisition of 20–40 frames using a 561-nm laser under TIRF illumination and an EMCCD camera with an EM gain of 400–600 at 5 Hz. This cycle of activation and acquisition was repeated between 150 and 300 times with the activation pulse duration increasing gradually during the experiment.

**sptPALM**—Cells, expressing photoactivatable mCherry-labeled SNAREs, were imaged in phenol red-free culture medium at 37 °C and 5% CO<sub>2</sub>, 95% air. Photoactivatable mCherry was activated with a brief pulse (1–40 ms) of 405-nm laser light under TIRF illumination followed by acquisition of 100 frames using a 561-nm laser under TIRF illumination and an EMCCD camera with an EM gain of 600–800 at 20 Hz. This cycle of activation and acquisition was repeated between 150 and 300 times with the activation pulse duration increasing gradually during the experiment.

**Vesicle Tracking and Fusion**—For vesicle tracking and stimulation experiments, PC12 cells, expressing Neuropeptide Y-EGFP, were maintained on the microscope at 37 °C and 5% CO<sub>2</sub>, 95% air. Cells were imaged in Krebs buffer (115 mM sodium chloride, 5 mM potassium chloride, 24 mM sodium bicarbonate, 2.5 mM calcium chloride, 1 mM magnesium chloride, 10 mM HEPES (pH 7.4), 0.1% (w/v) BSA) adjusted to 290 mosm. For stimulation, ATP was added during the recording to a final concentration of 300 mM. Secretory vesicle movement and fusion were acquired using a 491-nm laser under TIRF illumination and an EMCCD camera with an EM gain of 200–400 at 20 Hz.

### Image Analysis

**Single-molecule Localization**—For static PALM and GSDIM datasets, single molecules were detected using a Matlab routine kindly provided by Samuel Hess (Orono, ME) (25). For PALM datasets, individual frames between activation pulses were summed together using ImageJ before localization. Localized datasets were then used for further analysis in Matlab or rendered at high resolution. Rendering of localized molecules was performed using the same Matlab algorithms and false-colored in ImageJ.

<sup>3</sup> The abbreviations used are: TIRF, total internal reflection fluorescence; TIRFM total internal reflection fluorescence microscopy; PALM, photoactivatable localization microscopy; sptPALM, single particle tracking PALM; GSDIM, ground state depletion followed by individual molecule return microscopy; FRAP, fluorescence recovery after photobleaching; EMCCD, electron-multiplying charge-coupled device; EM gain, electron-multiplying gain; t-SNARE, target-SNARE; v-SNARE, vesicle-SNARE.

## Munc18-1 Molecules Move between Membrane Molecular Depots

**Single-molecule Localization Microscopy Analysis**—Following single-molecule localization, the spatial distribution of individual molecules was analyzed from the coordinate information. Ripley's analyses were performed using custom-written Matlab algorithms (21) as we reported previously. To compare the observed spatial distribution with the random state, the same number of molecules in the same spatial area was redistributed randomly 1000 times. For each simulation, the Ripley's K function and L transformation were derived. This is presented as light gray envelopes for the randomized simulations with the test case in black. Deviation of the test case above the envelopes at short radii indicates a nonrandom morphology with areas of high and low density. Deviation of the test case below the envelopes would indicate some form of minimum distance between adjacent molecules.

To analyze the spatial distribution of secretory vesicles relative to the SNARE molecules, nearest neighbor analysis was performed. Using the PALM coordinates of SNARE proteins and the centroid coordinates of secretory vesicles, SNARE molecules were assigned to their nearest vesicle using the nearest-neighbour routine in Matlab. A sampling radii was determined based on the range over which the t-SNAREs and v-SNARE would be able to interact using available structural information. Following allocation of molecules to their nearest secretory vesicle, the number of molecules within 82.5 nm of the centroid of each vesicle was determined.

**sptPALM Detection and Tracking**—An automated particle detection and tracking system has been developed and applied. The system combines particle detection in each single image frame and frame-to-frame particle correspondence implemented in Matlab. Particle detection in each single frame comprises three components: 1) particle probability image mapping, 2) refinement of particle probability image, and 3) particle segmentation. The first component is implemented by three steps. (a) The Haar-like feature for each pixel is measured in the original grayscale image. (b) A weak threshold is applied to the Haar-like feature to coarsely classify each pixel into one of two classes: particle or background. (c) A particle probability concept is defined as the ratio of the number of spatially connected particle pixels to the total number of pixels in a small region of a particle size. Particle features are significantly enhanced in the particle probability image. The second component is implemented by applying a rotationally symmetric Gaussian low pass filter to the newly obtained particle probability image to get more accurate particle probability at each pixel. The third component is implemented by firstly estimating existing regions of particles and their corresponding markers of particles from the refined particle probability image and then using the marker-controlled watershed transform to accurately segment the particle regions from the original grayscale image. Our particle detection algorithm allows for the detection of particle positions at a subpixel level and accurate estimation of particle topologies such as size and intensity. The robust frame-to-frame particle correspondence is finally implemented by incorporating these particle topologies into the system state vector of an interacting multiple model filter to better deal with particle motion modeling and robust data association. Here, three motion models, random walk, first order, and sec-

ond order linear extrapolations are used for motion modeling, and a dynamic programming algorithm is used to optimize the particle correspondence by minimizing the association cost function.

**FRAP Experiments**—Photobleaching was carried out in TIRF mode at 37 °C using an Olympus Cell<sup>^</sup>FRAP laser scanning head in conjunction with an Olympus Cell Excellence total internal reflection fluorescence microscopy (TIRFM) system. A circular bleach area of radius 1.06 μm was selected and bleached between frames 5 and 6 of 200, with a frame acquired every 31 ms. Bleaching was performed in the readout time of the camera, meaning that no interruption to imaging was required. ImageJ was used to extract intensity data from the resulting image files. These data consisted of the mean intensity with three circular regions of the image ( $r = 1.06 \mu\text{m}$ ): one ( $I_{\text{frap}}$ ) centered on the bleached region, one outside of the cell or sheet ( $I_{\text{back}}$ ), and one ( $I_{\text{ref}}$ ) in a region of the membrane remote from the bleach point.  $I_{\text{norm}}$  for each frame was calculated by correcting the  $I_{\text{frap}}$  value using the  $I_{\text{ref}}$  data, to account for the general photobleaching that occurs during acquisition, as well as normalizing to the prebleach values, according to Equation 1 below

$$I_{\text{norm}}(t) = \frac{I_{\text{ref\_pre}}}{I_{\text{ref}}(t) - I_{\text{back}}(t)} \times \frac{I_{\text{frap}}(t) - I_{\text{back}}(t)}{I_{\text{frap\_pre}}} \quad (\text{Eq. 1})$$

where  $I_{\text{norm}}(t)$  is the normalized intensity;  $I_{\text{frap}}(t)$  is the measured average intensity inside the bleached spot;  $I_{\text{ref}}(t)$  is the measured average reference intensity; and  $I_{\text{back}}(t)$  is the measured average background intensity outside the cell.  $_{\text{pre}}$  is the averaging of intensity in the corresponding Region of Interest before the bleach moment and after subtraction of background intensity.

Following the normalization of the data, the half-time of recovery for each curve was determined by using SigmaPlot (Scientific Computing Inc.) to fit the data with an equation of the form

$$I_{\text{norm}}(t) = a + \frac{b \times t}{t_{1/2} + t} \quad (\text{Eq. 2})$$

where  $a$  is the bleach point of the curve (*i.e.* relative intensity immediately after bleaching) and  $a+b$  is the maximum recovered relative fluorescence. Thus,  $b$  represents the mobile fraction of the molecules. This equation assumes that all the labeled molecules move according to the same profile, which may not be the case when proteins can interact with components of their surroundings (cytosolic proteins interacting with membrane-bound proteins, for example). The presence of two pools of protein with different mobilities was considered by fitting with a bimodal form of Equation 2.

$$I_{\text{norm}}(t) = a + \frac{c \times b_1 \times t}{t_{1/2(1)} + t} + \frac{c \times b_2 \times t}{t_{1/2(2)} + t} \quad (\text{Eq. 3})$$

In this case,  $a$  is still the bleach point of the curve, but  $c$  represents the total mobile fraction with  $b_1$  and  $b_2$  representing the percentage of the mobile fraction with  $t_{1/2(1)}$  and  $t_{1/2(2)}$  respectively.



## Munc18-1 Molecules Move between Membrane Molecular Depots

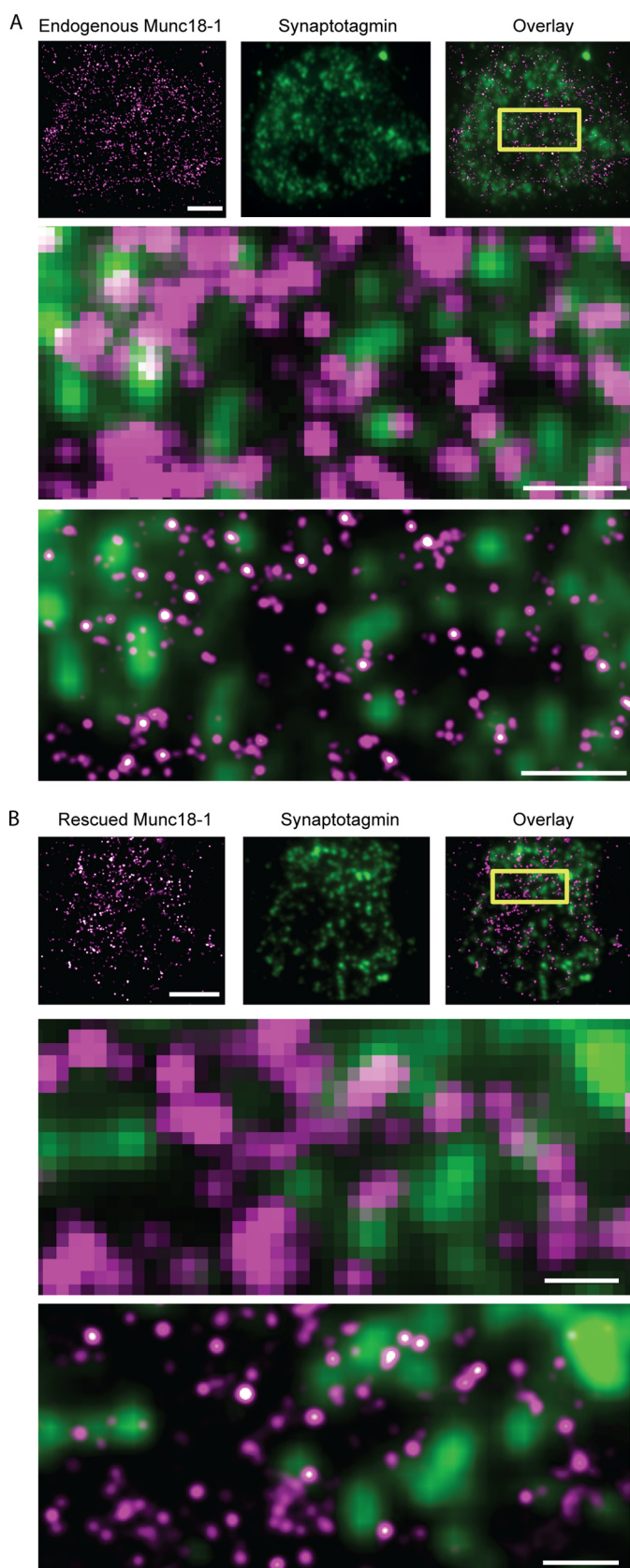


**FIGURE 1.** A, Munc18-1 molecules reside in depots distinct from secretory vesicles. TIRFM images of wild-type PC12 cells fixed and immunolabeled against both Alexa Fluor 647-Munc18-1 (left panel, magenta) and Alexa Fluor 488-synaptotagmin (middle panel) show single localized Munc18-1 molecules (scale bar, 5  $\mu\text{m}$ ) and labeled secretory vesicles (middle panel). An over-

lay image represents a merged image of single Munc18-1 molecules and secretory vesicles (right panel). A convolved GSDIM map of the boxed region of Alexa Fluor 647-Munc18-1 molecules is displayed to approximate a diffraction limited image and highlights that the majority of signals from secretory vesicles and Munc18-1 do not overlap; scale bar, 500 nm (upper zoom). A rendered map of single Munc18-1 molecules at a higher zoom within the boxed region (lower zoom) demonstrates the lack of co-clustering between Munc18-1 and secretory vesicles; scale bar, 500 nm. Areas of white indicate spatial overlap. B, KD43 PC12 cells functionally rescued with Munc18-1 were also fixed and immunolabeled with both Alexa Fluor 647-Munc18-1 (left panel, magenta) and Alexa Fluor 488-synaptotagmin (middle panel). Heterologous Munc18-1 was also found in areas of the plasma membrane not associated with membrane-proximal vesicles and adopted a distribution similar to the wild-type situation.

A curve was considered to be bimodal (*i.e.* the product of two pools moving at different rates) if Equation 3 provided a better fit to the data than Equation 2 (judged from the residuals of the fit and a reduced  $\chi$ -squared test). The difference in  $R^2$  value for each curve was calculated, and if the “unimodal”  $R^2$  value exceeded the bimodal  $R^2$  value for a curve, then it was assumed to consist of one pool, whereas if the bimodal  $R^2$  value was greater than the unimodal  $R^2$  value, the curve was deemed to consist of two independently moving pools.

The characteristic diffusion time  $t_{1/2}$  of a population is related to the diffusion coefficient  $D$  ( $\mu\text{m}^2/\text{s}$ ) by the following

$$D = \frac{\omega^2}{4 \times t_{1/2}} \quad (\text{Eq. 4})$$

where  $\omega$  is the radius of the bleach spot.

### RESULTS AND DISCUSSION

To probe the molecular organization of endogenous and heterologous Munc18-1 on a nanometer scale, we employed both GSDIM (22) and PALM (25). GSDIM involved immunodetecting decorated endogenous Munc18-1 with a fluorophore-conjugated antibody (Alexa Fluor 647) and driving this into a dark state using laser illumination in the presence of a reducing buffer. Single Alexa Fluor 647-conjugated antibodies, bound to immunodetected Munc18-1 molecules, spontaneously re-emerge from this dark state, permitting the localization of individual epitopes separated in a time stack (supplemental Fig. 1). Thus, wild-type PC12 cells were chemically fixed for 90 min to ensure complete immobilization (23) and subsequently processed for GSDIM. This revealed that endogenous Munc18-1 molecules displayed a heterogeneous distribution across the plasma membrane with molecules arranged into ensembles interspersed with largely single molecules, in agreement with recent findings describing the distribution of syntaxin molecules (26, 27) (Fig. 1A).

Munc18-1 is absolutely required for exocytosis and is thought to act at the final stages of vesicle fusion (12), but it remains unknown how it is spatially organized at the plasma membrane. Therefore we next decided to probe the spatial relationship between single endogenous Munc18-1 molecules and membrane-proximal secretory vesicles using GSDIM and TIRFM. Wild-type PC12 cells were fixed and processed for Munc18-1 GSDIM, whereas they were also co-immunostained against synaptotagmin 1 (an endogenous marker of the vesicular membrane). Surprisingly, these experiments revealed the preferential siting of Munc18-1 molecules in areas of the

lay image represents a merged image of single Munc18-1 molecules and secretory vesicles (right panel). A convolved GSDIM map of the boxed region of Alexa Fluor 647-Munc18-1 molecules is displayed to approximate a diffraction limited image and highlights that the majority of signals from secretory vesicles and Munc18-1 do not overlap; scale bar, 500 nm (upper zoom). A rendered map of single Munc18-1 molecules at a higher zoom within the boxed region (lower zoom) demonstrates the lack of co-clustering between Munc18-1 and secretory vesicles; scale bar, 500 nm. Areas of white indicate spatial overlap. B, KD43 PC12 cells functionally rescued with Munc18-1 were also fixed and immunolabeled with both Alexa Fluor 647-Munc18-1 (left panel, magenta) and Alexa Fluor 488-synaptotagmin (middle panel). Heterologous Munc18-1 was also found in areas of the plasma membrane not associated with membrane-proximal vesicles and adopted a distribution similar to the wild-type situation.

## Munc18-1 Molecules Move between Membrane Molecular Depots

plasma membrane that were largely devoid of secretory vesicles (Fig. 1A). Calculating how these image data would have appeared if imaged using diffraction-limited fluorescence microscopy resulted in an image demonstrating partial overlap between Munc18-1 and synaptotagmin (Fig. 1A).

Next we determined whether rescuing Munc18-1-silenced PC12 cells (clone KD43) with exogenously expressed, functional (21), fluorescent Munc18-1 recapitulated the endogenous, wild-type molecular distribution. GSDIM imaging of rescued KD43 PC12 cells expressing sufficient levels of heterologous Munc18-1 to fully restore exocytosis (comparable with wild-type levels (21)) also revealed Munc18-1 to be located in areas of the cell distinct from membrane-proximal vesicles and thus subject to similar targeting and localization to endogenous Munc18-1 (Fig. 1B).

Munc18-1 and syntaxin interact in two distinct conformations. Munc18-1 can bind and stabilize syntaxin in a closed conformation (2, 3), inconsistent with exocytosis, and also via its highly conserved N terminus (termed the “N-peptide” (4, 7, 28–30)); this interaction mode is thought to occur at or near the site of vesicle fusion. We have previously shown that disrupting specifically the interaction between Munc18-1 and the N-peptide of syntaxin resulted in a reduction in single-vesicle mobility and fusion capabilities (21). Therefore we went on to investigate whether these downstream effects on vesicle dynamics were a result of a concomitant change in the spatial arrangement of Munc18-1 molecules in relation to secretory vesicles. KD43 PC12 cells were co-transfected with Munc18-1[I127A] (known not to interact with the syntaxin N-peptide (21)) and syntaxin, fixed, and processed for Munc18-1 GSDIM and synaptotagmin 1 immunodetection as before. GSDIM imaging reported that Munc18-1[I127A] molecules were distributed heterogeneously, congregating in areas of the cell membrane that were not associated with secretory vesicles (supplemental Fig. 2). No difference was found between this molecular pattern and that of wild-type Munc18-1, suggesting that binding between Munc18-1 and the N-peptide of syntaxin is not involved in targeting Munc18-1 to defined sites or vesicles on the plasma membrane.

Although GSDIM data are invaluable for defining the spatial distribution of endogenous proteins, further statistical analysis of this is hampered at present by the fact that individual molecules may move reversibly from an “off” state to being repetitively fluorescent (supplemental Fig. 1) (22, 31). This means that single molecules may be counted multiple times in an analysis as the precise coordinate of each signal will vary on the nanoscale because of photon statistics and minute sample movements. To overcome these limitations and acquire statistical information on the spatial patterning of exogenously expressed Munc18-1 molecules, we next used PALM. PALM optically resolves fluorescent proteins to molecular resolution through the serial photo-activation and -irreversible destruction of subsets of molecules with each step optimized to ensure a sparse distribution of signals visible during each cycle (24, 25). Point spread function signals determined to arise from single molecules in the sample are localized, and the coordinates are added to a cumulative map. In this way, many thousands of single molecules are typically localized in a single experiment,

and this allows for further statistical spatial analysis of point patterns.

We first examined the localization of single photoactivatable molecules of Munc18-1 and Munc18-1[I127A] co-expressed alongside syntaxin in KD43 PC12 cells (supplemental Fig. 3). Positional information describing PA-mCherry-Munc18-1 and -Munc18-1[I127A] molecules was subsequently rendered into molecular maps, where Munc18-1 and Munc18-1[I127A] molecules were seen to adopt a heterogeneous distribution across the plasma membrane, recapitulating the endogenous molecular arrangement we previously determined (Fig. 1, supplemental Fig. 2). To analyze the spatial arrangement of Munc18-1 molecules, we used Ripley’s K function (32) followed by its L function transformation to compare the spatial distribution of the individual molecules with a randomized sample (constrained to the same particle number and area as the test sample). Both Munc18-1 and Munc18-1[I127A] exhibited a clustered, nonrandom distribution across the plasma membrane of secretion-competent rescued PC12 cells (Fig. 2A). This finding demonstrates that Munc18-1 is subject to a higher order organization at the molecular level, a finding previously shown with the t-SNAREs (26, 27). Performing reciprocal PALM experiments revealed that perturbing the syntaxin N-terminal interaction with Munc18-1 had no effect on the syntaxin nonrandom, highly ordered distribution (supplemental Fig. 4). Thus, targeted disruption of the Munc18-1-syntaxin-N-terminal interaction resulted in a reorganization of *interaction* with syntaxin, as we showed previously (21), with no change in the molecular spatial pattern at the plasma membrane (supplemental Fig. 4).

It can be deduced from our current understanding that for Munc18-1 to act at the final stage of fusion, it must be associated with syntaxin (and probably the other SNAREs) and an adjacent vesicle for exocytosis to proceed. Although PALM imaging can never provide an exact measure of the number of molecules in a sample, as it is not certain that every molecule has been localized, it can provide a lower limit for the number of molecules per unit area (26). Using PALM and assigning *xy* coordinates to all single Munc18-1 molecules and labeled secretory vesicles, it was possible to quantify statistically the nanoscale organization of single Munc18-1 molecules in relation to their nearest secretory vesicle center, also with nanometer certainty (Fig. 2B). KD43 PC12 cells rescued with fluorescently labeled Munc18-1, syntaxin, and NPY, a vesicle cargo protein, were fixed and imaged using PALM. These newly assembled, NPY-labeled vesicles are trafficked preferentially to the plasma membrane, have the highest probability of fusion, and comprise at least in part the readily releasable pool (33). These vesicles were also localized using TIRFM, allowing visualization only within a 90-nm distance of a refractive index interface, thereby selectively localizing only “morphologically docked” membrane-proximal vesicles.

Using this cellular system, we determined the average numbers of detected Munc18-1 molecules within 200 nm from the center of mass of each vesicle (*i.e.* under the equatorial diameter of a secretory vesicle), finding that the average number of detected Munc18-1 molecules localized under a single vesicle ranged between zero and a maximum of nine (Fig. 2C;  $n =$



## Munc18-1 Molecules Move between Membrane Molecular Depots

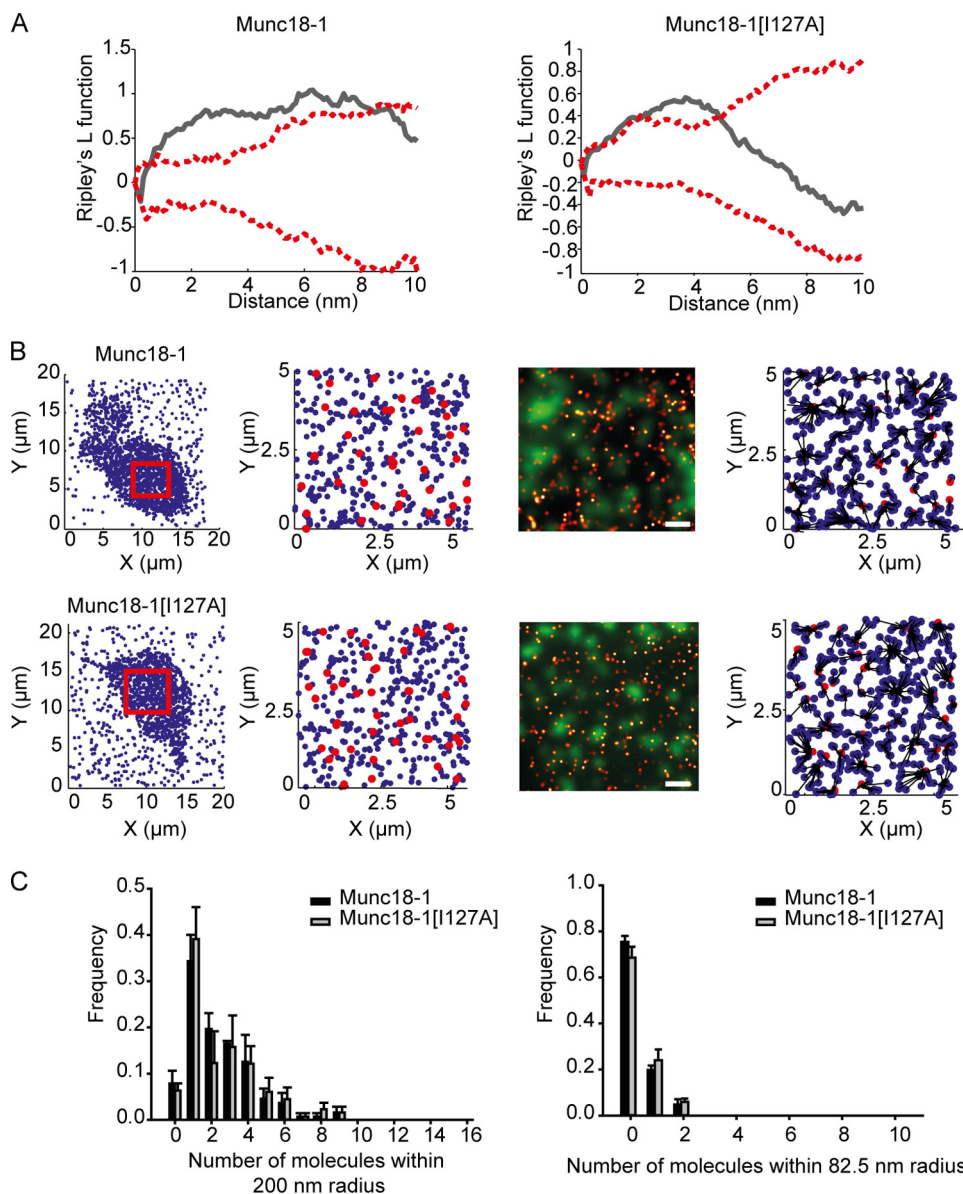


**FIGURE 2. Small numbers of Munc18-1 molecules are associated with single vesicles.** *A*, representative L-function plots (gray lines) are shown for cells rescued with Munc18-1 and Munc18-1[I127A]. Each representative dataset, consisting of *xy* coordinates describing the localization of individual Munc18-1 molecules (certain to  $<12$  nm), was repeatedly randomized, and the L-function was re-derived. Confidence envelopes, showing the maximum and minimum L-function values from 1000 randomizations, are shown (dashed red lines). Munc18-1 and Munc18-1[I127A] are distributed in a nonrandom, organized manner across the plasma membrane. *B*, KD43 PC12 cells were transfected with Munc18-1, syntaxin, and a fluorescent vesicle cargo marker, NPY-EGFP, and fixed 48 h later. Single Munc18-1 molecules were activated and localized, and the positions of single Munc18-1 molecules (blue) and secretory vesicles were centroided (red; left and middle left panels). Middle right panels, TIRFM image showing NPY-EGFP-labeled secretory vesicles and a rendered map of single Munc18-1 molecules within the boxed region at the plasma membrane. Individual molecules were assigned to a nearest neighbor secretory vesicle. The “quiver” diagram shows single-molecule coordinates (red spots) connected by to the centroid coordinates of their closest vesicle (right panels). *C*, a nearest neighbor algorithm was used to calculate the number of Munc18-1 molecules within 200 nm (i.e. a vesicle radius) or 82.5 nm (i.e. the chord distance calculated from the maximum v-SNARE and t-SNAREs interaction length, see “Results”) of a secretory vesicle center. No significant differences exist between Munc18-1 (black bars) and Munc18-1[I127A] (gray bars) cell data. Error bars are S.E. (Munc18-1 expressing 12,778 molecules, 866 vesicles,  $n = 7$  cells; Munc18-1[I127A] expressing 10,548 molecules, 740 vesicles,  $n = 8$  cells).

24,096 Munc18-1 molecules localized to 412 vesicles,  $n = 8$  independent experiments). Using recent structural data describing SNARE proteins in lipid bilayers (34, 35), the maximum separation distance over which the t- and v-SNARE proteins can physically interact was calculated to be 17.8 nm. Combining this estimate with the assumption that plasma and vesicular membranes are immediately adjacent (previously used to define “docked” secretory vesicles by electron microscopy (36)), we calculated that the maximum radius from the

center of a secretory vesicle at which the t-SNARE and v-SNARE proteins could interact was 82.5 nm. These values therefore provide the most stringent criteria for measuring the maximum distance over which SNARE proteins are able to interact with a neighboring vesicle to catalyze its fusion. This analysis demonstrated that each morphologically docked vesicle only had a 25% probability of being physically associated with one or two Munc18-1 molecules in this functionally rescued cellular system (Fig. 2C). Furthermore, neither the prob-

## Munc18-1 Molecules Move between Membrane Molecular Depots

ability of having a detected Munc18-1 molecule associated with a secretory vesicle nor the number of molecules found to reside under a single vesicle was altered upon N-terminal interaction disruption (Fig. 2C;  $n = 20,567$  Munc18-1[I127A] molecules, localized to 350 vesicles,  $n = 7$  experiments). An important caveat here is that we cannot set an upper bound on the number of molecules detected using these approaches. We think it unlikely that there is a large reservoir of undetected Munc18-1 for the following reasons; the GSDIM of endogenous Munc18-1 molecules and PALM of heterologous Munc18-1 (sufficient to functionally rescue our null system) appear similar. The GSDIM of untagged Munc18-1 in our knockdown cells appears similar to wild-type cells (*i.e.* largely distinct from vesicle docking sites). In this experiment, Munc18-1 overexpression at this level was sufficient to rescue secretion to wild-type levels. In addition, these data are in strong agreement with our recent finding (43) that the t-SNAREs are also distributed across regions of the membrane distinct from docked vesicles. These findings are in agreement with several biophysical studies that suggested that very few SNARE molecules are required to catalyze exocytosis (37, 38), but contrast with most imaging studies, which tend to suggest that the SNARE proteins are concentrated into dense molecular clusters underneath vesicles (23, 39–41). Viewed with diffraction-limited convolution, our single-molecule data also give rise to apparent molecular clusters that overlap partially with vesicles, illustrating the importance of super-resolution imaging.

Chemically fixing cells is a requirement for acquiring the most accurate positional information of single molecules but results in a loss of information regarding the molecular kinetics and processes existing within a biological system. Furthermore, such fixation and antibody staining may lead to artifacts such as antibody-induced epitope clustering. It has been reported that syntaxin exists in excess over Munc18-1, leading to the idea that Munc18-1 molecules may service multiple syntaxins by moving between binding sites on the membrane (4). To test this, we next determined the mobility and spatiotemporal behaviors of individual Munc18-1 molecules in living KD43 PC12 cells by analyzing large cohorts of single molecules using single particle tracking PALM (sptPALM (19)). Data are acquired in the same manner as for PALM, but with reduced activation energy (to activate fewer molecules at once), faster image frame rates, and lower excitation power, to ensure a larger number of image frames before single molecules bleach off. Single particle tracking approaches may then be used to quantify molecular movements. Large cohorts of single Munc18-1 ( $n = 5873$ ) and Munc18-1[I127A] ( $n = 20,878$ ) molecules were tracked at living plasma membranes at 37 °C, revealing kinetically and spatially distinct populations of molecules (Fig. 3, A and B). To provide a large-scale quantitative representation of the dynamics of Munc18-1 at the plasma membrane of intact, living cells, contour maps were created by plotting the kinetic behaviors of single Munc18-1 molecules over every pixel. Tracking thousands of Munc18-1 and Munc18-1[I127A] molecules revealed heterogeneities across the plasma membrane, with molecules favoring particular plasma membrane “hot spots” or depots (Fig. 4A). Statistical analyses of sptPALM data revealed that Munc18-1 molecules diffuse freely across the plasma mem-

brane but display restricted, slower motions in areas with more Munc18-1 molecules (Fig. 4A). Conversely, Munc18-1 molecules travel at greater speeds between these molecular depots. The anticorrelation between molecular density and speed was confirmed with spatial resolution using difference plots (Fig. 4A); together with our previous data (43) showing Munc18-1 and syntaxin binary interaction in membranes (16, 21, 31, 44), we conclude that Munc18-1 interacts with syntaxin in hotspots distinct from vesicle docking sites. This conclusion is further supported by our recent findings (43) that the majority of t-SNARE molecules of syntaxin1a and SNAP-25 are spatially distinct from secretory vesicle docking sites. Furthermore, modeling of t-SNARE molecule mobilities, spatial distributions, and densities, combined with similar measurements of vesicular dynamics, predicted that single vesicles, on average, encounter few t-SNAREs simultaneously. Our findings here demonstrate that Munc18-1 molecules have similar mean velocities to syntaxin1a molecules (supplemental Fig. 5) as well as indistinguishable spatial distributions. Importantly, however, our super-resolution imaging cannot define whether Munc18-1 and syntaxin physically interact at the plasma membrane. To address this, we used two different approaches: time-correlated single photon counting fluorescence lifetime imaging and fluorescence recovery after photobleaching (FRAP). The former technique detected and quantified Förster resonance energy transfer (FRET) in domains near the plasma membrane of living cells, confirming an intermolecular proximity consistent with a direct protein-protein interaction between syntaxin1 and Munc18-1 as we previously published (29, 30). Time-correlated single photon counting fluorescence lifetime imaging, although providing direct quantitative data describing FRET, suffers from a slow acquisition time and relatively low axial resolution, meaning that it is difficult to be sure that the data are acquired from the plasma membrane and not the cytoplasm. To overcome these caveats, we employed FRAP combined with TIRFM with rapid data acquisition. This approach allowed us to image and quantify molecular diffusion rates of syntaxin1a and Munc18-1 simultaneously within a 70-nm optical section at the base of the cells, with a millisecond time resolution (Fig. 5, A and B). We found that although syntaxin1a molecules exhibit a single, slow diffusion rate consistent with a trans-membrane protein, Munc18-1 molecules exhibit two distinct diffusional behaviors: one not statistically different from that determined for syntaxin1a and another, significantly faster rate (Fig. 5, C–E). These two mobilities could be deconvolved, revealing that ~75% of Munc18-1 resided in the slow pool, with the remaining 25% moving near the plasma membrane at rates inconsistent with being bound to a membrane protein (Fig. 5, F and G). Taken together, these data from a range of independent experimental approaches lead us to conclude that Munc18-1 molecules interact with syntaxin1a in morphologically heterogeneous regions of dense molecular accumulations, distinct from vesicle docking sites.

Diffusion maps of Munc18-1 reflect the dynamics of molecules in single cells. By combining data from multiple experiments, we constructed a histogram of track angle, frequency, and molecular speed (supplemental Fig. 5), which demonstrated that a large fraction of Munc18-1 molecules exhibited a



## Munc18-1 Molecules Move between Membrane Molecular Depots

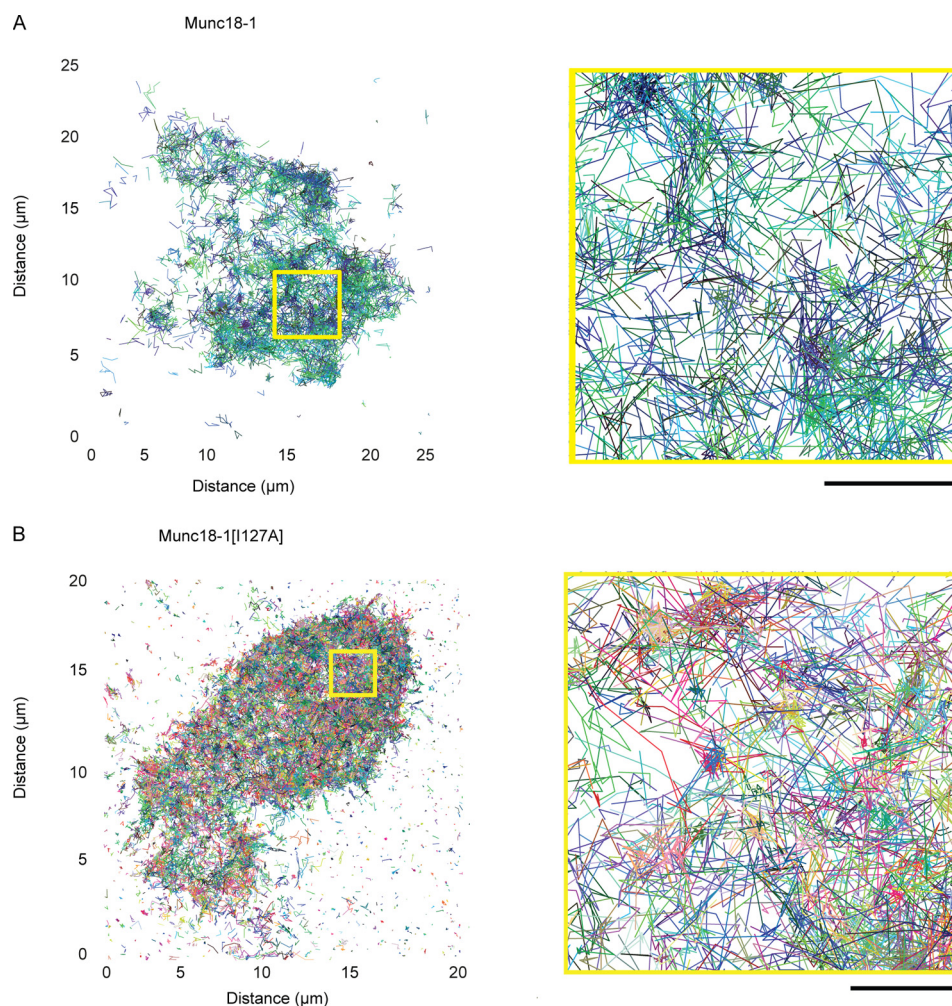


FIGURE 3. **Munc18-1 molecular dynamics at the living plasma membrane.** KD43 PC12 cells were transfected with PA-Munc18-1 and syntaxin1a for 48 h and then subjected to live PALM imaging and single particle tracking. Molecules visible for more than 90 ms (three frames) were tracked using in-house Matlab algorithms. *A* and *B*, images of molecular tracks of single molecules in KD43 PC12 cells expressing either Munc18-1 (*panel A*;  $n = 5,873$  molecules) or Munc18-1[I127A] (*panel B*;  $n = 20,878$  molecules). Track multicolor is to improve contrast. Scale bar, 2  $\mu\text{m}$ . The boxed area is zoomed for each representative cell (*right panels*). Expanded image scale bar is 500 nm. Tracking large cohorts of single Munc18-1 molecules recapitulates the fixed cell data, demonstrating a heterogeneous dynamic molecular distribution across the membrane plane.

highly restricted speed, with a mean velocity of  $0.091 \mu\text{m s}^{-1}$  at the plasma membrane (Munc18-1  $n = 31,566$  molecules,  $n = 3$  cells; Munc18-1[I127A]  $n = 40,078$  tracks,  $n = 3$  cells). This finding suggests that almost all membrane-proximal Munc18-1 is associated with syntaxin1a, as expected, as the molecular velocities agree with those measured for integral membrane proteins as opposed to cytosolic factors using fluorescence correlation spectroscopy (data not shown) (45). Perturbing the N-terminal interaction between Munc18-1 and syntaxin had no effect on the molecular speed of Munc18-1, indicating that the syntaxin N-peptide is not critical in the maintenance of Munc18-1 at the plasma membrane, but is required for initial recruitment (32). The spatiotemporal organization of relatively immobile Munc18-1 molecules into hot spots, distinct from vesicle docking sites but interspersed with more mobile molecules, is suggestive of Munc18-1 molecules moving between membrane depots. We addressed this question using single particle tracking statistical analysis, finding that Munc18-1 molecules move in a directed way across the membrane (Fig. 4, *B* and *C*). Although Brownian motion is superimposed on all

molecular dynamics, the “wind diagram” in Fig. 4*C* illustrates that there is an average directionality in each sampled region (including hundreds of single-molecule tracks) between molecular hotspots that is inconsistent with pure Brownian behavior. Exemplar trajectories of 50 representative molecular tracks from both Munc18-1 and Munc18-1[I127A] molecules confirmed that molecules move between areas of high molecular densities (Fig. 4*C*).

Munc18-1 is variously thought of as an important factor in the process of SNARE trafficking (14–16, 26), vesicle docking (8, 9, 46, 47), and priming (9, 10) acting at the point of membrane fusion (12, 32, 48), or not (11, 29, 47, 49). This controversy is due, in part, to the lack of available data describing directly how Munc18-1 and SNARE proteins are structurally organized and dynamically regulated on the molecular level relative to secretory vesicles in cells.

Here, we show that the majority of vesicles have no detected proximal Munc18-1 molecule within a functionally relevant distance, suggesting either that very few Munc18-1 molecules are required for exocytosis to proceed or that Munc18-1 is not



## Munc18-1 Molecules Move between Membrane Molecular Depots

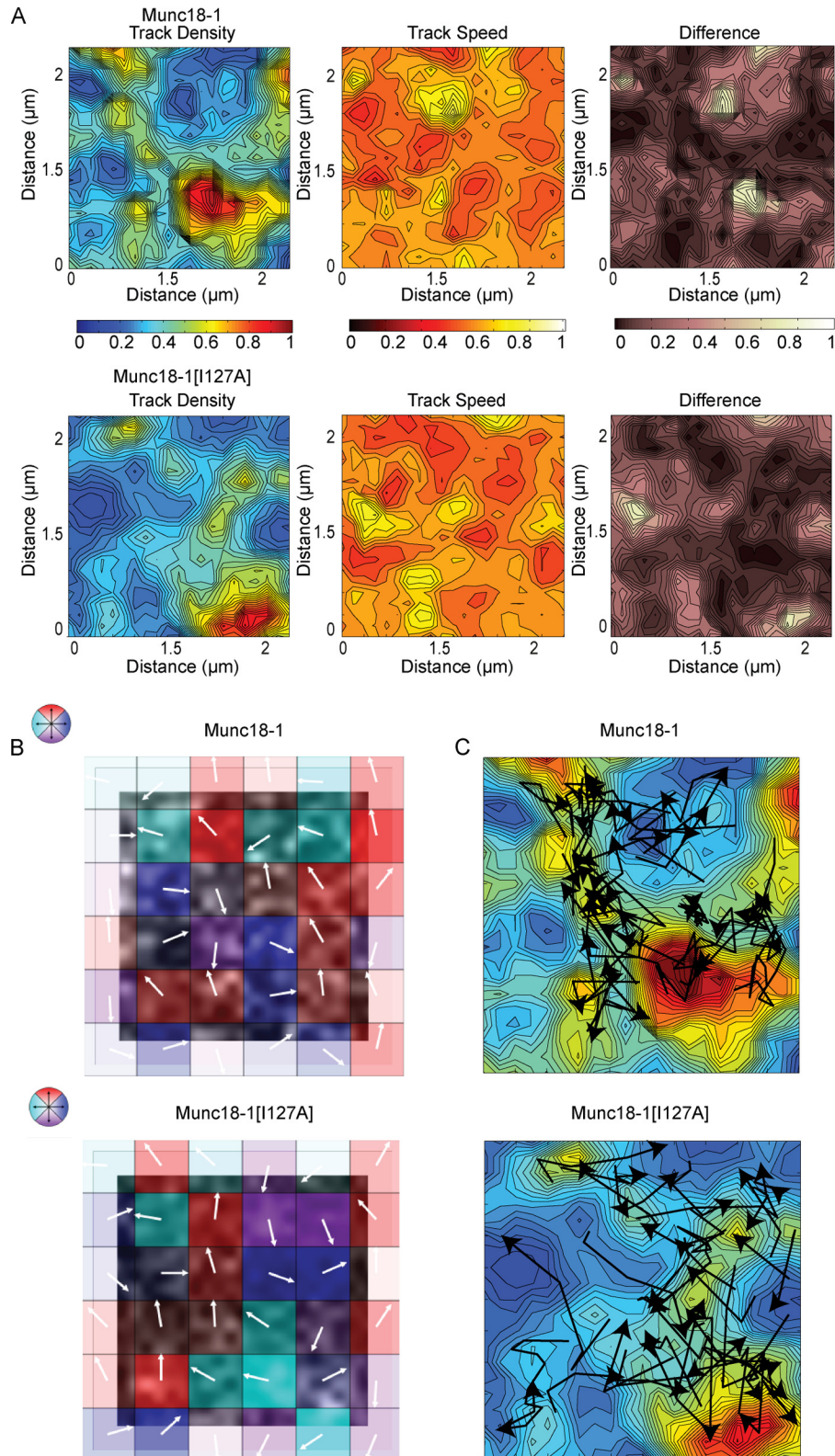


**FIGURE 4. Munc18-1 molecules move between molecular depots at the plasma membrane.** *A*, KD43 PC12 cells were transfected with either PA-Munc18-1 or PA-Munc18-1[I127A] and syntaxin1a for 48 h and then subjected to live PALM imaging and single particle tracking. Contour maps containing normalized molecular densities and speeds are shown. Difference contour maps were created by calculating the difference between the density and molecular speed across each pixel of the image. All corresponding images are on the same color scale, and the contour map corresponds to the region of interest from cells displayed in Fig. 3. *B*, directionality maps were generated and show the average direction of Munc18-1 (786 tracks, upper panel) or Munc18-1[I127A] (1239 tracks, lower panel) molecules within each 500-nm square. Squares are color-coded in terms of direction. *C*, representative single trajectories of 50 Munc18-1 (upper panel) and Munc18-1[I127A] (lower panel) molecules are superimposed onto molecular density contour maps. Single molecules move between areas of high molecular concentrations.

## Munc18-1 Molecules Move between Membrane Molecular Depots

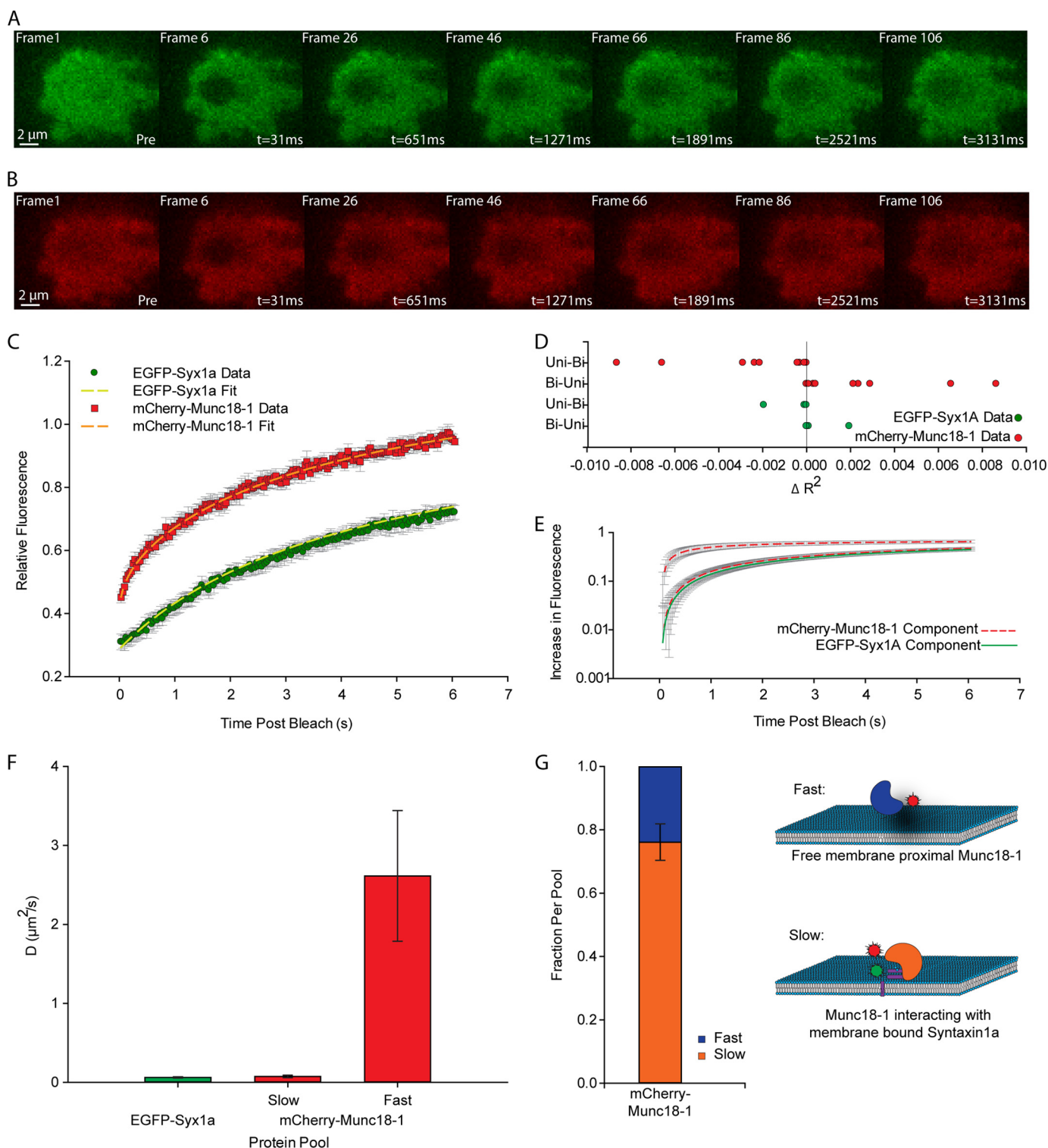


**FIGURE 5. Two pools of Munc18-1 molecules at the plasma membrane.** *A* and *B*, representative montage of frames from a single FRAP experiment on a cell expressing EGFP-syntaxin1a (*A*) and mCherry-Munc18-1 (*B*). Photobleaching of a circle of radius  $1.06 \mu\text{m}$  was carried out between frames 5 and 6, and frame 6, the “bleach moment,” is considered as  $t = 0$ . *C*, average normalized fluorescence recovery curves from EGFP-syntaxin1a (*green circles*) and mCherry-Munc18-1 (*red squares*). *Dotted lines* represent the average fit of the data with the most applicable equation (single or double hyperbolic function). *Error bars* represent S.E.,  $n = 9$ . *D*, determination of bimodal diffusion by  $R$ -squared evaluation of residuals ( $R^2 = (\text{residual sum of squares})/(\text{total sum of squares})$  for a dataset). When the  $R$ -squared value of the bimodal fit exceeded that of the unimodal fit (*i.e.* Bi – Uni  $> 0$ , where Bi represents bimodal and Uni represents unimodal), it was considered a better fit, and the data were classed as containing two populations. This was the case for the majority of the Munc18-1 data. *E*, average fits of separated components of single-mode EGFP-syntaxin1a (*solid green line*) diffusion and bimodal mCherry-Munc18-1 diffusion (*dashed red lines*). *Error bars* represent S.E.,  $n = 9$ . *F*, diffusion rates of separated components of single-mode EGFP-syntaxin1a and bimodal mCherry-Munc18-1 motions. *Error bars* represent S.E.,  $n = 9$ . *G*, *left panel*, relative distribution of Munc18 molecules between fast-moving cytosolic and slow-moving syntaxin1a-bound pools. *Error bars* represent S.E.,  $n = 9$ . *Right panel*, graphic summarizing our FRAP conclusions. Plasma membrane-proximal Munc18-1 exists predominantly as a relatively immobile syntaxin1a-bound pool with a smaller ( $\sim 25\%$  of total) pool of more mobile, unbound molecules.



required at the final stage of fusion. It is known that only a minority of vesicular cargo is released even in response to a maximal stimulation. It is tempting to speculate that the majority of vesicles have the incorrect complement of secretory machinery molecules to support fusion, meaning that most vesicles and their cargo are never released. It is impossible to combine the millisecond-rate imaging required to capture single fusion events with the timescale of minutes required for single-molecule localization microscopies at the moment; however, the mathematical model we recently published (43) has started to incorporate the quantitative information delivered by these new super-resolution imaging approaches and supports this hypothesis.

We show that single Munc18-1 molecules exhibit different diffusional behaviors, spatially organized across the plasma membrane of live neuroendocrine cells. Single Munc18-1 molecules were seen to freely explore the plasma membrane, preferring specific areas of the planar bilayer in agreement with our fixed sample data, evidenced by a heterogeneous density of tracks. Munc18-1 molecules within molecular depots exhibited reduced speed suggestive of a molecular interaction, consistent with the finding that syntaxin is also confined in nanodomains on the cell surface (40, 41, 50). Furthermore, we also found that most Munc18-1 molecules do not reside within interaction distance of a membrane-proximal vesicle. Despite the population of cells exhibiting full secretion, at the single-vesicle level, most vesicles remain unused as observed previously (33), and the reason for this remains unknown. Currently, single-molecule imaging is incompatible with imaging of single-vesicle exocytosis as the two modalities operate on very distinct timescales, so substantial further work will be required to combine these approaches. We hypothesize, however, that the precise molecular complement underneath individual vesicles, possibly determined by interaction with the lipid environment (50), dictates fusion probability and that many vesicles will reside in areas of the membrane incapable of supporting fusion.

### REFERENCES

- Söllner, T., Whiteheart, S. W., Brunner, M., Erdjument-Bromage, H., Geromanos, S., Tempst, P., and Rothman, J. E. (1993) SNAP receptors implicated in vesicle targeting and fusion. *Nature* **362**, 318–324
- Pevsner, J., Hsu, S. C., and Scheller, R. H. (1994) n-Sec1: a neural-specific syntaxin-binding protein. *Proc. Natl. Acad. Sci. U.S.A.* **91**, 1445–1449
- Dulubova, I., Sugita, S., Hill, S., Hosaka, M., Fernandez, I., Südhof, T. C., and Rizo, J. (1999) A conformational switch in syntaxin during exocytosis: role of munc18. *EMBO J.* **18**, 4372–4382
- Rickman, C., Medine, C. N., Bergmann, A., and Duncan, R. R. (2007) Functionally and spatially distinct modes of munc18-syntaxin 1 interaction. *J. Biol. Chem.* **282**, 12097–12103
- Shen, J., Tareste, D. C., Paumet, F., Rothman, J. E., and Melia, T. J. (2007) Selective activation of cognate SNAREpins by Sec1/Munc18 proteins. *Cell* **128**, 183–195
- Dulubova, I., Khvotchev, M., Liu, S., Huryeva, I., Südhof, T. C., and Rizo, J. (2007) Munc18-1 binds directly to the neuronal SNARE complex. *Proc. Natl. Acad. Sci. U.S.A.* **104**, 2697–2702
- Burkhardt, P., Hattendorf, D. A., Weis, W. I., and Fasshauer, D. (2008) Munc18a controls SNARE assembly through its interaction with the syntaxin N-peptide. *EMBO J.* **27**, 923–933
- Voets, T., Toonen, R. F., Brian, E. C., de Wit, H., Moser, T., Rettig, J., Südhof, T. C., Neher, E., and Verhage, M. (2001) Munc18-1 promotes large dense-core vesicle docking. *Neuron* **31**, 581–591
- Gulyás-Kovács, A., de Wit, H., Milosevic, I., Kochubey, O., Toonen, R., Klingauf, J., Verhage, M., and Sørensen, J. B. (2007) Munc18-1: sequential interactions with the fusion machinery stimulate vesicle docking and priming. *J. Neurosci.* **27**, 8676–8686
- Deák, F., Xu, Y., Chang, W.-P., Dulubova, I., Khvotchev, M., Liu, X., Südhof, T. C., and Rizo, J. (2009) Munc18-1 binding to the neuronal SNARE complex controls synaptic vesicle priming. *J. Cell Biol.* **184**, 751–764
- Gerber, S. H., Rah, J.-C., Min, S.-W., Liu, X., de Wit, H., Dulubova, I., Meyer, A. C., Rizo, J., Arancillo, M., Hammer, R. E., Verhage, M., Rosenmund, C., and Südhof, T. C. (2008) Conformational switch of syntaxin-1 controls synaptic vesicle fusion. *Science* **321**, 1507–1510
- Fisher, R. J., Pevsner, J., and Burgoyne, R. D. (2001) Control of fusion pore dynamics during exocytosis by Munc18. *Science* **291**, 875–878
- Rowe, J., Corradi, N., Malosio, M. L., Taverna, E., Halban, P., Meldolesi, J., and Rosa, P. (1999) Blockade of membrane transport and disassembly of the Golgi complex by expression of syntaxin 1A in neurosecretion-incompetent cells: prevention by rbSEC1. *J. Cell Sci.* **112**, 1865–1877
- Rowe, J., Calegari, F., Taverna, E., Longhi, R., and Rosa, P. (2001) Syntaxin 1A is delivered to the apical and basolateral domains of epithelial cells: the role of munc-18 proteins. *J. Cell Sci.* **114**, 3323–3332
- Arunachalam, L., Han, L., Tassew, N. G., He, Y., Wang, L., Xie, L., Fujita, Y., Kwan, E., Davletov, B., Monnier, P. P., Gaisano, H. Y., and Sugita, S. (2008) Munc18-1 is critical for plasma membrane localization of syntaxin 1 but not of SNAP-25 in PC12 cells. *Mol. Biol. Cell* **19**, 722–734
- Medine, C. N., Rickman, C., Chamberlain, L. H., and Duncan, R. R. (2007) Munc18-1 prevents the formation of ectopic SNARE complexes in living cells. *J. Cell Sci.* **120**, 4407–4415
- Yildiz, A., Forkey, J. N., McKinney, S. A., Ha, T., Goldman, Y. E., and Selvin, P. R. (2003) Myosin V walks hand-over-hand: single fluorophore imaging with 1.5-nm localization. *Science* **300**, 2061–2065
- Teramura, Y., Ichinose, J., Takagi, H., Nishida, K., Yanagida, T., and Sako, Y. (2006) Single-molecule analysis of epidermal growth factor binding on the surface of living cells. *EMBO J.* **25**, 4215–4222
- Manley, S., Gillette, J. M., Patterson, G. H., Shroff, H., Hess, H. F., Betzig, E., and Lippincott-Schwartz, J. (2008) High-density mapping of single-molecule trajectories with photoactivated localization microscopy. *Nat. Methods* **5**, 155–157
- Graham, M. E., Barclay, J. W., and Burgoyne, R. D. (2004) Syntaxin/Munc18 interactions in the late events during vesicle fusion and release in exocytosis. *J. Biol. Chem.* **279**, 32751–32760
- Smyth, A. M., Rickman, C., and Duncan, R. R. (2010) Vesicle fusion probability is determined by the specific interactions of munc18. *J. Biol. Chem.* **285**, 38141–38148
- Fölling, J., Bossi, M., Bock, H., Medda, R., Wurm, C. A., Hein, B., Jakobs, S., Eggeling, C., and Hell, S. W. (2008) Fluorescence nanoscopy by ground-state depletion and single-molecule return. *Nat. Methods* **5**, 943–945
- Sieber, J. J., Willig, K. I., Kutzner, C., Gerding-Reimers, C., Harke, B., Donnert, G., Rammner, B., Eggeling, C., Hell, S. W., Grubmüller, H., and Lang, T. (2007) Anatomy and dynamics of a supramolecular membrane protein cluster. *Science* **317**, 1072–1076
- Betzig, E., Patterson, G. H., Sougrat, R., Lindwasser, O. W., Olenych, S., Bonifacino, J. S., Davidson, M. W., Lippincott-Schwartz, J., and Hess, H. F. (2006) Imaging intracellular fluorescent proteins at nanometer resolution. *Science* **313**, 1642–1645
- Hess, S. T., Girirajan, T. P. K., and Mason, M. D. (2006) Ultra-high resolution imaging by fluorescence photoactivation localization microscopy. *Biophys. J.* **91**, 4258–4272
- Rickman, C., Medine, C. N., Dun, A. R., Moulton, D. J., Mandula, O., Halemani, N. D., Rizzoli, S. O., Chamberlain, L. H., and Duncan, R. R. (2010) t-SNARE protein conformations patterned by the lipid microenvironment. *J. Biol. Chem.* **285**, 13535–13541
- Bar-On, D., Wolter, S., van de Linde, S., Heilemann, M., Nudelman, G., Nachliel, E., Gutman, M., Sauer, M., and Ashery, U. (2012) Super-resolution imaging reveals the internal architecture of nano-sized syntaxin clusters. *J. Biol. Chem.* **287**, 27158–27167
- Misura, K. M., Scheller, R. H., and Weis, W. I. (2000) Three-dimensional structure of the neuronal-Sec1-syntaxin 1a complex. *Nature* **404**, 355–362
- Rickman, C., and Duncan, R. R. (2010) Munc18/Syntaxin interaction ki-

- netics control secretory vesicle dynamics. *J. Biol. Chem.* **285**, 3965–3972
30. Rathore, S. S., Bend, E. G., Yu, H., Hammarlund, M., Jorgensen, E. M., and Shen, J. (2010) Syntaxin N-terminal peptide motif is an initiation factor for the assembly of the SNARE-Sec1/Munc18 membrane fusion complex. *Proc. Natl. Acad. Sci. U.S.A.* **107**, 22399–22406
  31. McEvoy, A. L., Greenfield, D., Bates, M., and Liphardt, J. (2010) Q&A: Single-molecule localization microscopy for biological imaging. *BMC Biol.* **8**, 106
  32. Ripley, B. D. (1977) Modelling spatial patterns. *J. R. Soc. Series B Stat. Methodol.* **39**, 172–192
  33. Duncan, R. R., Greaves, J., Wiegand, U. K., Matskevich, I., Bodammer, G., Apps, D. K., Shipston, M. J., and Chow, R. H. (2003) Functional and spatial segregation of secretory vesicle pools according to vesicle age. *Nature* **422**, 176–180
  34. Ellena, J. F., Liang, B., Wiktor, M., Stein, A., Cafiso, D. S., Jahn, R., and Tamm, L. K. (2009) Dynamic structure of lipid-bound synaptobrevin suggests a nucleation-propagation mechanism for trans-SNARE complex formation. *Proc. Natl. Acad. Sci. U.S.A.* **106**, 20306–20311
  35. Stein, A., Weber, G., Wahl, M. C., and Jahn, R. (2009) Helical extension of the neuronal SNARE complex into the membrane. *Nature* **460**, 525–528
  36. de Wit, H., Walter, A. M., Milosevic, I., Gulyás-Kovács, A., Riedel, D., Sørensen, J. B., and Verhage, M. (2009) Synaptotagmin-1 docks secretory vesicles to syntaxin-1/SNAP-25 acceptor complexes. *Cell* **138**, 935–946
  37. Mohrmann, R., de Wit, H., Verhage, M., Neher, E., and Sørensen, J. B. (2010) Fast vesicle fusion in living cells requires at least three SNARE complexes. *Science* **330**, 502–505
  38. Sinha, R., Ahmed, S., Jahn, R., and Klingauf, J. (2011) Two synaptobrevin molecules are sufficient for vesicle fusion in central nervous system synapses. *Proc. Natl. Acad. Sci. U.S.A.* **108**, 14318–14323
  39. Lang, T., Bruns, D., Wenzel, D., Riedel, D., Holroyd, P., Thiele, C., and Jahn, R. (2001) SNAREs are concentrated in cholesterol-dependent clusters that define docking and fusion sites for exocytosis. *EMBO J.* **20**, 2202–2213
  40. Barg, S., Knowles, M. K., Chen, X., Midorikawa, M., and Almers, W. (2010) Syntaxin clusters assemble reversibly at sites of secretory granules in live cells. *Proc. Natl. Acad. Sci. U.S.A.* **107**, 20804–20809
  41. Knowles, M. K., Barg, S., Wan, L., Midorikawa, M., Chen, X., and Almers, W. (2010) Single secretory granules of live cells recruit syntaxin-1 and synaptosomal associated protein 25 (SNAP-25) in large copy numbers. *Proc. Natl. Acad. Sci. U.S.A.* **107**, 20810–20815
  42. Deleted in proof
  43. Yang, L., Dun, A. R., Martin, K. J., Qiu, Z., Dunn, A., Lord, G. J., Lu, W., Duncan, R. R., and Rickman, C. (2012) Secretory vesicles are preferentially targeted to areas of low molecular SNARE density. *PLoS One* **7**, e49514
  44. Kim, S. A., Sanabria, H., Digman, M. A., Gratton, E., Schwille, P., Zipfel, W. R., and Waxham, M. N. (2010) Quantifying translational mobility in neurons: comparison between current optical techniques. *J. Neurosci.* **30**, 16409–16416
  45. Oh, E., Kalwat, M. A., Kim, M.-J., Verhage, M., and Thurmond, D. C. (2012) Munc18-1 regulates first-phase insulin release by promoting granule docking to multiple syntaxin isoforms. *J. Biol. Chem.* **287**, 25821–25833
  46. de Wit, H., Cornelisse, L. N., Toonen, R. F., and Verhage, M. (2006) Docking of secretory vesicles is syntaxin dependent. *PLoS ONE* **1**, e126
  47. Martin-Verdeaux, S., Pombo, I., Iannascoli, B., Roa, M., Varin-Blank, N., Rivera, J., and Blank, U. (2003) Evidence of a role for Munc18-2 and microtubules in mast cell granule exocytosis. *J. Cell Sci.* **116**, 325–334
  48. Meijer, M., Burkhardt, P., de Wit, H., Toonen, R. F., Fasshauer, D., and Verhage, M. (2012) Munc18-1 mutations that strongly impair SNARE-complex binding support normal synaptic transmission. *EMBO J.* **31**, 2156–2168
  49. Lang, T., Margittai, M., Hölzler, H., and Jahn, R. (2002) SNAREs in native plasma membranes are active and readily form core complexes with endogenous and exogenous SNAREs. *J. Cell Biol.* **158**, 751–760
  50. van den Bogaart, G., Meyenberg, K., Risselada, H. J., Amin, H., Willig, K. I., Hubrich, B. E., Dier, M., Hell, S. W., Grubmüller, H., Diederichsen, U., and Jahn, R. (2011) Membrane protein sequestering by ionic protein–lipid interactions. *Nature* **479**, 552–555